Tailoring selectivity of electrochemical hydrogen peroxide generation by tunable pyrrolic-nitrogen-carbon

Laiquan Li, Cheng Tang, Yao Zheng, Bingquan Xia, Xianlong Zhou, Haolan Xu, Shi-Zhang Qiao*

L. Li, Dr. C. Tang, Dr. Y. Zheng, B. Xia, X. Zhou, Prof. S. Z. Qiao

School of Chemical Engineering and Advanced Materials

The University of Adelaide

SA 5005, Australia
E-mail: s.qiao@adelaide.edu.au

Prof. H. Xu
Future Industries Institute

University of South Australia

SA 5095, Australia

Electrochemical reduction of O_2 via two-electron reaction pathway to H_2O_2 provides possibility for replacing the current anthraquinone process, enabling sustainable and decentralized H_2O_2 production. Here, a nitrogen-rich few-layered graphene (N-FLG) with tunable nitrogen configuration was developed for electrochemical H_2O_2 generation. A positive correlation between the content of pyrrolic-N and the H_2O_2 selectivity was experimentally observed. The critical role of pyrrolic-N was elucidated by the variable intermediate adsorption profiles as well as the dependent negative shifts of the pyrrolic-N peak on x-ray adsorption near edge structure spectra. By virtue of the optimized N doping configuration and the unique porous structure, the as-fabricated N-FLG electrocatalyst exhibited a high selectivity towards electrochemical H_2O_2 synthesis as well as superior long-term stability. To achieve high-value products on both anode and cathode electrodes with optimized energy efficiency, a practical device coupling electrochemical H_2O_2 generation and furfural oxidation was assembled, simultaneously enabling a high yield rate of H_2O_2 at cathode (9.66 mol h^{-1} g_{cat}^{-1}) and 2-furoic acid at anode (2.076 mol m^{-2} h^{-1}) under a small cell voltage of 1.8 V.

1. Introduction

Hydrogen peroxide (H_2O_2) is one of the most important industrial chemicals as a potential energy carrier and an environmentally friendly oxidant for various sanitization applications and environmental remediation.[1-4] Nowadays, the large-scale manufacturing of H_2O_2 is dominated by the multi-step anthraquinone process, which is energy-intensive, waste-producing and difficult for on-site H_2O_2 production.[4-6] Development of low-cost and decentralized H_2O_2 production is thus highly desired to reduce the cost for H_2O_2 synthesis, storage and transportation. Recently, the oxygen electrochemistry strategy is developed as an attractive and alternative approach for on-site and on-demand H_2O_2 production, in that oxygen undergoes a two-electron pathway reduction.[7-11] Moreover, the electrochemical H_2O_2 generation can be coupled with many other reactions, for example biomass conversion reactions, enabling the production of high-value products on both anode and cathode of the practical device within small energy input.

For H_2O_2 synthesis from two-electron oxygen reduction reaction (ORR), it requires an active and low-cost electrocatalyst which can selectively reduce O_2 to H_2O_2 instead of H_2O. It has been reported that ORR on some noble metals and their alloys such as Pt,[12] Au,[13] Pd,[14] Pd-Hg,[15] and Au-Pd[16] follows a two-electron pathway with small overpotential as well as high H_2O_2 selectivity. However, the large-scale applications of noble metals are far more constrained by their scarcity. Carbon-based materials are therefore particularly promising due to their abundance, low cost and high electrochemical stability under reaction conditions.[8] More importantly, the tunable surface and structure properties make it possible to modify the electrochemical performance of the carbon-based electrocatalysts.[17-19] Among various modification methods, nitrogen doping is of particular interest to induce efficient active sites with favourable electrochemical properties.[20, 21] However, the majority of these previous works have shown that N-doped carbon based electrocatalysts are prone to accelerate the four-electron ORR pathway under alkaline conditions.[22, 23] There is still

limited understanding in identifying and tailoring the active nitrogen configuration for two-electron ORR pathway.

The two-electron pathway involves only one intermediate, namely OOH*, while further reduction of OOH* results in other two intermediates (O* and OH*), leading to a four-electron pathway.[24, 25] Probing the adsorbed intermediates on the surface of electrocatalysts during the electrochemical process could provide meaningful information in terms of the active sites and reaction pathways.[26] Generally, mixed two-electron and four-electron pathways usually occur due to the lack of optimal electronic structure for either of them.[27] To suppress the four-electron pathway, the key knob relies on preventing the bond-breaking reaction of OOH* + e^- → O* + OH^-, and thus effectively preserving the OOH* intermediate.[24, 28] For example, Au surfaces with relatively weak oxygen binding energy could efficaciously prevent the breakage of the O–OH* bond, resulting in a highly selective two-electron pathway for H_2O_2 production.[29] Hence, it is highly desirable to develop a catalyst platform with fine tunability in electronic structure for regulating the intermediate binding energy and ORR pathway, as well as improving the catalytic activities.

Herein, we elaborately designed a scalable g-C_3N_4-templated strategy to synthesize N-rich few-layered graphene (N-FLG) with tunable nitrogen doping and dependent activities towards H_2O_2 electrosynthesis. Using melamine and glycine as nitrogen sources for different nitrogen configurations, the nitrogen doping state on as-fabricated N-FLG could be effectively tuned by varying the mass ratio of the precursors. We experimentally observed a positive correlation between the content of the pyrrolic-N and the H_2O_2 selectivity. The critical role of the pyrrolic-N on two-electron ORR pathway was further elucidated by x-ray adsorption near edge structure (XANES) spectroscopy. Profiting from the optimized N configuration and the porous structure, the as-fabricated N-FLG-8 (mass ratio of melamine:glycine is 8) electrocatalyst exhibited excellent two-electron ORR performance in alkaline medium with high selectivity over 95% towards electrochemical H_2O_2 synthesis as well as superior long-term stability. When coupled with biomass

conversion reaction (furfural oxidation), a practical device was assembled with the generation of high-value products (H_2O_2 on cathode and 2-furoic acid on anode) at high yield rates under a small cell voltage.

2. Results and Discussion

2.1. Material Synthesis and Characterization

As illustrated in **Figure 1**a, we synthesized the N-FLG-X by grinding a mixture of melamine and glycine with a mass ratio of X:1, followed by a two-step polymerization and carbonization under Ar atmosphere. During the pyrolysis process, the melamine would transfer to melam, melem and finally to $g-C_3N_4$, resulting in nitrogen configurations in forms of pyridinic- and graphitic-N.[30] Meanwhile, the dehydration process of glycine would occur on the *in-situ* formed $g-C_3N_4$, resulting in a significant amount of N−H bond,[31] which is expected to contribute to the formation of pyrrolic-N. Therefore, the nitrogen configuration on the final product would be adjusted by varying the mass ratio of melamine and glycine. It is noteworthy to mention that the *in-situ* formed $g-C_3N_4$, which exhibits layered and lamellar structure (Figure S1), could serve as a template for the final products. When the melamine was absent or in relatively low mass ratios, the glycine was prone to agglomerate into bulk lumps with low specific surface areas (Figure S2a-c). When a higher mass ratio of melamine was applied, a well-defined porous graphene-like material with plenty of wrinkles could be obtained (Figure S2d). For a fair comparison with similar nanostructure, here we adopted mass ratios of 8:1, 12:1, and 16:1, and the as-fabricated materials were denoted as N-FLG-8, N-FLG-12, and N-FLG-16, respectively. Figure 1b-d present scanning electron microscope (SEM) image and the bright-field transmission electron microscope (TEM) images of N-FLG-8 as a typical sample. With the help of the $g-C_3N_4$ template, the precursors transform into ultrathin graphene layers with a crumpled and wrinkle-rich morphology (Figure 1b and c). The graphene layers are abundant of in-plane holes with size less than 10 nm, and exhibit thickness of about six layers (Figure 1d). It is notable that the interplanar spacing is ~0.44 nm, which is much larger than the theoretical thickness of monolayer

graphene (0.335 nm).[32] This can be further verified by the x-ray diffraction (XRD) pattern. As shown in Figure S3, all the N-FLG samples exhibit a broad peak located at ~25.6°, which is lower than the (002) peak (26.6°) of the standard graphite (JCPDS No. 26-1079). The enlarged interlayer distance can be attributed to the N-rich feature of the graphene layers,[33, 34] which is expected to facilitate the mass transfer during the fast electrochemical reactions. The energy dispersive spectroscopy (EDS) element mapping of N-FLG-8 (Figure S4) suggests the homogeneous incorporation of N in the graphene nanosheets. N-FLG-12 and N-FLG-16 are also demonstrated to possess the similar 2D wrinkle-rich nanostructure (Figure S5 and S6). The structural porosity was further investigated by nitrogen adsorption-desorption experiments (Figure S7-S9). A high specific surface area of 358.8 m^2 g^{-1} is achieved for N-FLG-8, which is comparable to those of N-FLG-12 (372.5 m^2 g^{-1}) and N-FLG-16 (397.0 m^2 g^{-1}). Besides, the pore width of all the obtained graphene materials is mainly distributed within 2~10 nm, which is consistent with the TEM observations and further confirms their porous feature. The Raman spectra reveal similar intensity ratio of D and G bands (I_D/I_G) for N-FLG-8, N-FLG-12 and N-FLG-16, indicating their comparable defective contents (Figure S10). Moreover, the similar double layer capacitances of the three samples reveal their analogous roughness of the electrode surface with small differences in electrochemically active surface area (Figure S11).

The chemical properties of the N-FLG samples were then investigated in detail by x-ray photoelectron spectroscopy (XPS) and XANES spectroscopy. As shown in Figure S12 and Table S1, the XPS survey spectra reveal a high content of nitrogen in all samples (19.2 at.% for N-FLG-8, 18.1 at.% for N-FLG-12, and 16.5 at.% for N-FLG-16), demonstrating their N-rich feature. The high nitrogen doping content is expected to effectively alter the electronic structure and facilitate the O_2 adsorption.[35] As displayed in **Figure 2**a, the N 1s XPS spectra can be deconvoluted into four peaks, which are assigned to pyridinic-N (398.4 eV), pyrrolic-N (399.6 eV), graphitic-N (401.1 eV) and oxidized-N (402.7 eV).[27, 36, 37] It is obvious that the percentage of pyrrolic-N significantly decreases from 24.9% for N-FLG-8 to 8.1% for N-FLG-16, while those of pyridinic-N and graphitic-N increase

from 30.6% to 40.1% and 34.8% to 43.0%, respectively (Table S2). Besides, from N-FLG-8 to N-FLG-16, the gradually decreased content of C–N bond and the increased content of C=N bond displayed in the high resolution C 1s XPS spectra also reveal the same trend for the nitrogen configuration variation (Figure S13, Table S3). It is further verified by the normalized N 1s K edge XANES spectra. As revealed in Figure 2b, a distinct decrease of pyrrolic-N from N-FLG-8 to N-FLG-16 is obviously observed, which is consistent with the XPS results. More specifically, from N-FLG-8 to N-FLG-16, the atomic content of pyrrolic-N significantly decreases from 4.8 at.% to 1.3 at.%, while those of pyridinic-N and graphitic-N slightly increase from 5.8 at.% to 6.6 at.%, and from 6.6 at.% to 7.1 at.%, respectively (Figure 2c, Table S2). Therefore, by virtue of the *in-situ* formed g-C_3N_4 as a template, we obtained hierarchical few-layered nitrogen-rich graphene materials with abundant in-plane pores, which are believed to enhance the mass transfer during the electrochemical reaction.[19, 21] In addition, due to the different polymerization processes, the nitrogen configuration was selectively tuned by varying the mass ratio of the nitrogen precursors. Compared with the conventional tuning method by controlling the annealing temperature,[38] our method provides a more controllable and effective approach for selectively modifying the nitrogen configuration on carbon materials with similar nanostructures. It is expected to serve as a decent material platform for studying the structure-activity relation of N-doped carbon electrocatalyst at atomic level.

2.2. Electrocatalytic ORR Performances

The ORR performances were evaluated in 0.10 M KOH using rotation ring disk electrode (RRDE), with the collection efficiency being pre-calibrated by the redox reaction of $[Fe(CN_6)]_4^-$/$[Fe(CN_6)]_3^-$.[39] **Figure 3**a shows the linear sweep voltammetry (LSV) curves collected at 1600 rpm in O_2-saturated electrolyte, together with the H_2O_2 detection current collected by the Pt ring electrode at a constant potential of 1.2 V vs. reversible hydrogen electrode (RHE). The background current that arises from double layer capacitance was subtracted by recording the sweep profile at the same scan rate in N_2-saturated electrolyte. In the order from N-FLG-16, N-FLG-12, to N-FLG-8, increased ring currents,

decreased disk currents, and negatively shifted onset potentials are obtained, suggesting a gradually tuned reaction pathway with a higher fraction of two-electron ORR. The calculated H_2O_2 selectivity and electron transfer number (n) are plotted in Figure 3b as a function of applied potential. N-FLG-8 delivers the highest H_2O_2 selectivity of over 95% and the lowest electron transfer number below 2.1 in a wide potential range from 0.30 V to 0.70 V vs. RHE. Such a high selectivity and activity towards electrochemical H_2O_2 generation is superior to most of the previously reported results (Figure S14, Table S4). H_2O_2 selectivity of ~80% and ~65% are observed on N-FLG-12 and N-FLG-16, respectively, suggesting that the nitrogen configuration could effectively tune the O_2-to-H_2O_2 selectivity. Accordingly, from N-FLG-8 to N-FLG-16, the electron transfer number is tuned from 2.01 to 2.81. Besides the good performance in alkaline solution, N-FLG-8 also exhibits decent H_2O_2 generation performance with a high selectivity of ~80% in a neutral solution (Figure S15). The electrochemical stability of N-FLG-8 was then evaluated using both RRDE test and bulk electrolysis. As shown in Figure 3c, the H_2O_2 selectivity could be maintained over 95% during 8 h continuous electrolysis at a fixed disk potential of 0.40 V vs. RHE. Nearly identical LSV curves were obtained before and after the stability test (Figure 3d), with 98.5% of the H_2O_2 selectivity and 98.2% of the disk current being maintained (Figure 3e). When coated onto a gas diffusion layer (GDL) electrode and tested in a H-type cell, N-FLG-8 can deliver a steady-state current density as high as –20 mA cm^{-2} over 50 h (Figure S16), demonstrating its excellent electrochemical stability and promising potential for practical applications.

2.3. The Activity Origin of H_2O_2 Generation

In spite of the similar nanostructure and specific surface area, obvious differences of ORR activity and selectivity are achieved on different N-FLG samples, which should be ascribed to the tuned

nitrogen configurations. Although oxygen doping has also been reported to facilitate the two-electron ORR process,[40, 41] we claim that the nitrogen doping instead of oxygen doping plays the determining role in our case because of the much lower atomic contents (Table S1) and similar configuration of oxygen dopants among all the three samples (Figure S17). It is notable that nitrogen-doped carbon materials have been widely reported as superior four-electron ORR electrocatalysts,[22, 23] while they can also serve as highly selective two-electron ORR electrocatalysts.[20, 42, 43] The exact correlation between the N doping configuration and the ORR pathway remains controversial, which limits the rational material design and performance optimization. Herein, we performed XANES spectroscopic characterization to probe the reaction intermediates and identify the real active sites for electrochemical H_2O_2 generation on N-FLG. **Figure 4**a-c present the evolution of the carbon K edge XANES spectra of N-FLG-8, N-FLG-12 and N-FLG-16 before and after ORR process. On the basis of previous reports,[44-48] the peak located at ~287.5 eV is related to $\pi^*_{C-O=C, C-N}$ in the pristine sample before reaction, and the intensity increment after reaction can be assigned to the adsorption of intermediate species (O*) on carbon atoms (Figure 4a-c).[45] Besides, the peak located at ~289.3 eV is attributed to the adsorption of OOH* intermediates.[45, 46] Generally, the OOH* intermediate evolves in both two-electron and four-electron pathways, while the O* intermediates only emerges in four-electron pathways. As shown in Figure 4a-c, N-FLG-8 exhibits the strongest intensity of C–OOH* peak and the lowest increment of C–O* peak after ORR, demonstrating its excellent selectivity towards two-electron ORR. Conversely, the significant increment of C–O* peak and the hardly any expansion of C–OOH* peak after ORR indicate a higher fraction of four-electron pathway process on N-FLG-16. This phenomenon can also be verified by the oxygen K edge XANES spectra, in which a distinct C–O* peak for N-FLG-16 while only a little increment for N-FLG-8 compared with the pristine spectra are observed after ORR (Figure S18).[48] Nitrogen K edge XANES spectra were further recorded to unravel the critical role of specific nitrogen configurations. As depicted in Figure 4d, we observed negative shifts of the pyrrolic-N peak after ORR, while the peak positions of the pyridinic-N and graphitic-N remained

nearly unchanged for all the three samples. The negative shift can be ascribed to the distortion of heterocycles caused by the absorption of intermediates on the carbon atoms near the pyrrolic-N.[45] Remarkably, the negative shifts in nitrogen K edge spectra descend in the order: N-FLG-8 (0.20 eV) > N-FLG-12 (0.16 eV) > N-FLG-16 (0.14 eV), in well consistence with the intensities of the C–OOH* peaks in carbon K edges. Thus, it is rational to conclude that the adsorption of OOH* intermediates on the carbon atoms near the pyrrolic-N induces the distortion of heterocycles and results in the negative shifts of the pyrrolic-N peak. Furthermore, when correlating the atomic content of specific nitrogen configurations with H_2O_2 selectivity, a positive relationship between the pyrrolic-N content and the H_2O_2 selectivity is obtained (Figure 4e), whereas no such positive correlation can be found for either pyridinic-N or graphitic-N (Figure S19).

It suggests that the much larger number of pyrrolic-N dopants in N-FLG-8 may alter the electronic structure towards optimized adsorption of OOH* intermediate and thus lead to the superior selectivity of two-electron pathway. To further understand the promoting effect of pyrrolic-N on selective H_2O_2 generation, we then measured LSV in a H_2O_2-containing (50 mmol L^{-1}) electrolyte. As shown in Figure S20, the H_2O_2 reduction current decreases obviously on N-FLG-8 compared to N-FLG-12 and N-FLG-16, indicating an effectively hindered reduction of H_2O_2 to H_2O due to the presence of more pyrrolic-N dopants. It has been reported that nitrogen atoms with a higher electronegativity could activate π-conjugated system and impart positive charge on the adjacent carbon atoms, thus facilitating the adsorption of OOH* intermediates.[49] However, the delocalized lone pair electrons from the pyridinic-N could aggressively induce charge transfer from the π orbital to the antibonding orbitals in O_2, resulting in significantly weakened O–O bond and further dissociation of OOH* intermediate into O* and OH*.[20, 50, 51] The graphitic-N is reported to be positively charged and the carbon atoms surrounding graphitic-N may act as Lewis acids,[52] which are not favourable for the adsorption of intermediates. Therefore, we propose that the OOH* intermediates could be substantially preserved with the presence of a high amount of pyrrolic-N,

leading to a two-electron ORR pathway on the adjacent carbon atoms. Four-electron pathway is supposed to preferentially occur on the carbon atoms adjacent to the pyridinic-N rather than pyrrolic-N dopants (Figure 4f).

2.4. Practical Device Demonstration

To investigate the potential of the catalyst for practical application, we combined the electrochemical H_2O_2 generation with biomass conversion for the purpose of producing valuable products on both cathode and anode. Furfural (FU), which is generally mass-produced by the dehydration of agricultural by-products,[53, 54] was here chosen as a substrate for electrochemical oxidation. The product of furfural oxidation, 2-furoic acid (FA), is widely used for preservative in industry, acting as bactericide and fungicide.[53, 54] The combination of H_2O_2 generation and FU oxidation was realized in a conventional flow cell with a two-electrode configuration (**Figure 5**a and Figure S21). A GDL electrode (1.8 × 1.8 cm^2) casted with N-FLG-8 electrocatalyst was used as the cathode electrode and a nickel foam was used as the anode electrode. The accumulated H_2O_2 yield on the cathode was quantified by Ce^{4+}/Ce^{3+} colorimetric method (the standard curve is shown in Figure S22), while the FA produced on the anode was determined by high performance liquid chromatography (HPLC). Figure 5b shows the polarization curves of the assembled flow cell with and without the presence of FU. Significantly increased current density and decreased cell voltage can be realized when replacing conventional oxygen evolution reaction (OER) by FU oxidation on the anode. Only a small cell voltage of 1.28 V, in contrast to 1.98 V in the absence of FU, is required to drive a high current density of 50 mA cm^{-2}, indicating the remarkable thermodynamic advantage of FU oxidation relative to water oxidation. Under the optimized mass transfer in flow cell setup, the cell current can reach as high as 350 mA (~110 mA cm^{-2}) at the cell voltage of 1.8 V (Figure 5b).

Bulk electrolysis was then performed at different cell voltages of 0.9, 1.2, 1.5 and 1.8 V. As shown in Figure 5c, H_2O_2 yield rate of 9.66 mol h^{-1} g$_{cat}^{-1}$ (2.31 mmol h^{-1} cm^{-2}) can be achieved at the cell voltage of 1.8 V, which outperforms most of the reported bulk H_2O_2 production in flow cell system

(Table S5). It is noteworthy to mention that high faradaic efficiencies of near 100% are realized at all the applied cell voltages, further demonstrating the exclusive selectivity for two-electron ORR pathway on N-FLG-8. This novel electrochemical device can be steadily operated for a long term with a stable current and product yield rate (Figure 5d, Figure S23). Simultaneously, the continuous consumption of FU and production of FA on the anode were also confirmed by the HPLC results (Figure S24). A high FU conversion rate of ~70% in 60 min with an average FA yield rate of 2.076 mol m^{-2} h^{-1} was achieved at the cell voltage of 1.8 V (Figure 5d).

3. Conclusion

In summary, porous N-rich few-layered graphene with controllable morphology, nanostructure and composition have been fabricated by a facile g-C_3N_4-templated method. By changing the mass ratio of the precursor materials, the content of pyrrolic-N was selectively tuned. We revealed that the H_2O_2 selectivity could be effectively facilitated with the presence of the high amount of pyrrolic-N. The critical role of the pyrrolic-N was elucidated by the variable adsorption profiles of OOH* and O* intermediates on C K edge XANES spectra as well as the dependent negative shifts of the pyrrolic-N peak on N K edge XANES spectra. N-FLG-8 with the highest pyrrolic-N content and abundant in-plane pores was demonstrated to have superior activity towards electrochemical H_2O_2 synthesis, enabling high selectivity over 95% and excellent long-term stability. By virtue of the high activity of N-FLG-8, a practical device coupling electrochemical H_2O_2 generation with furfural oxidation was assembled, enabling simultaneous production of value-added products of H_2O_2 on cathode with a high yield rate of 9.66 mol h^{-1} g_{cat}^{-1} (2.31 mmol h^{-1} cm^{-2}) and FA on anode with a yield rate of 2.076 mol m^{-2} h^{-1} under a small cell voltage of 1.8 V. The selective nitrogen configuration tuning method and the identification of the favourable effect of pyrrolic-N to two-electron ORR pathway in this work provide new ideas for the design of advanced carbon-based electrocatalysts for various electrochemical and catalytic applications.

4. Experimental Section

Synthesis of N-FLG: In a typical procedure, melamine and glycine with various mass ratios (for example 8:1 for N-FLG-8) was first thoroughly grinded in an agate mortar. The mixed powders were put into a porcelain boat and then transferred to a tube furnace. The mixture was first heated to 550 °C in Ar atmosphere at a ramp rate of 2 °C min^{-1}. After keeping at 550 °C for 2 h, the annealing temperature was then elevated to 800 °C with a ramp rate of 3 °C min^{-1} and kept at 800 °C for another 2 h. After cooling down naturally to room temperature, the resultant black product was grounded into powder using an agate mortar and directly used for the preparation of catalyst ink.

Imaging and spectroscopic characterization: Field-emission scanning electron microscope (SEM) images were collected on a FEI QUANTA 450 electron microscope. The TEM images, HAADF-STEM images and EDS mapping were collected on a FEI Titan Themis 80-200 operating at 200 kV. XRD patterns were obtained using a Rigaku MiniFlex 600 X-Ray Diffractometer with Co Kα radiation. XPS data were collected under ultrahigh vacuum (< 10^{-8} Torr) using a monochromatic Al Kα X-ray source. Raman data were collected on a HORIBA LabRAM HR Evolution spectroscopy using the excitation wavelength of 532 nm. The absorbance data of spectrophotometer were collected on SHIMADZU UV-2600 ultraviolet-visible (UV-Vis) spectrophotometer. Furfural and its oxidation product (2-furoic acid) were quantitatively determined by HPLC (Waters Alliance e2695 Separations Module).

Electrochemical measurements: Electrochemical data were collected with a CHI 760e electrochemical workstation (CHI Instruments, Inc.). Three-electrode system was used in the electrochemical measurement in which an Ag/AgCl electrode was used as the reference electrode, a graphite rod as a counter electrode, and a RRDE (disk area: 0.247 cm^2) with a Pt ring (ring area: 0.1866 cm^2) as the working electrode. All potentials measured against Ag/AgCl electrode were converted to the RHE. To prepare the catalyst ink, 5.0 mg of the obtained catalyst powders and 0.5 mg of carbon black were dispersed in 960 μL of the mixture of isopropanol and water (v/v=1:1) and 40 μL of 5 wt.% Nafion solution. After ultrasonic treatment for 3 h, 5.0 μL of the catalyst ink was drop-casted on to the disk electrode for the RRDE measurement.

The oxygen reduction activity was measured by cyclic voltammetry (CV) and LSV techniques in O_2 saturated electrolyte at a scan rate of 5.0 mV s^{-1}. Prior to the measurement, the Pt ring was first electrochemically cleaned by sweeping the potential between 0~0.8 V until steady CV curve was obtained. The electrolyte was first purged with N_2 and a LSV curve was recorded in N_2-saturated 0.10 M KOH at the rotating speed of 1600 rpm. Then, the electrolyte was purged with O_2 at least 30 min, and the LSV curve of ORR was collected in O_2-saturated 0.10 M KOH at the rotating speed of 1600 rpm. The capacitance or faradaic currents were then eliminated by subtracting the current measured in N_2-saturated electrolyte from that in O_2-saturated electrolyte. The ring currents were recorded by fixing the ring potential at 1.2 V vs. RHE to detect the H_2O_2 produced on disk electrode. The collection efficiency (*N*) was determined to be 37.1% by the redox reaction of $[Fe(CN)_6]^{4-}/[Fe(CN)_6]^{3-}$. Selectivity of the catalysts toward H_2O_2 production was calculated based on the following equation:

$$H_2O_2\% = \frac{200 \times I_{ring}/N}{|I_{disk}| + I_{ring}/N}$$

The electron transfer number at the disk electrode during ORR process was calculated as follows:

$$n = \frac{4|I_{disk}|}{|I_{disk}| + I_{ring}/N}$$

X-ray absorption near-edge structure (XANES) measurement: The K-edge x-ray absorption spectra of C, N and O were measured on the soft x-ray spectroscopy beamline at the Australian Synchrotron. For the XANES measurements, the catalyst powder was supported on a porous copper foam under ~10 Ton pressure. The copper foams with catalyst powder were first injected to an ultrahigh vacuum chamber to collect the pristine spectra. For the XANES spectra after ORR process, the electrodes were then reacted at a fixed potential of 0.6 V vs. RHE in an O_2 saturated 0.10 M KOH for 60 min. After the ORR process, the copper foam with catalysts was quickly dried by blowing Ar and subjected to the ultrahigh vacuum chamber for the data collection.

Measurement of electrochemically active surface area: The electrochemically active surface area was measured by double layer capacitance method. CV scans were conducted at the potential window from –0.05 V to 0.05 V vs. Ag/AgCl reference electrode with scan rates of 5, 10, 15, 20, and 25 mV s^{-1}. By plotting the $(J_a–J_c)/2$ at 0 V against the scan rate, the slope value was calculated to be the double layer capacitance (C_{dl}).

Practical device assembly and measurement: As shown in Figure S21, a conventional flow cell was constructed to simulate a practical device, which couples electrochemical H_2O_2 generation with furfural oxidation. 40 mL of 1.0 M KOH solution with 30 mmol L^{-1} of furfural continuously flows through the anode chamber which is separated from the cathode chamber by a Nafion 117 membrane (Fuel Cell store). A nickel foam (4 cm^2) was used as the anode electrode for furfural oxidation. The catalyst was dispersed onto a GDL electrode (1.8 × 1.8 cm^2) by a spray gun, resulting in a loading mass of 0.24 mg cm^{-2}. The cathode chamber was circulated with 40 mL of 1.0 M KOH under a flow rate of ~4 mL min^{-1}. High purity O_2 was continuously purged through the opposite side of the catalyst with a flow rate of ~5 mL min^{-1}. LSV was performed at a scan rate of 10.0 mV s^{-1} with a cell voltage range from 0 to 2.0 V. The electrolysis was then carried out by employing different cell voltages for various durations to evaluate the actual production of H_2O_2. All the LSV measurements and bulk electrolysis for the flow cell are carried out without IR compensation.

Product quantification: A Ce^{4+} titration method was used to quantitatively analyse the produced H_2O_2 based on the following equation:

$$2Ce^{4+} + H_2O_2 \rightarrow 2Ce^{3+} + 2H^+ + O_2 \uparrow$$
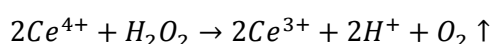
where the Ce^{4+} solution displays yellow while the Ce^{3+} solution is colorless. The yield of H_2O_2 was then quantified by measuring the mole amount of the consumed Ce^{4+}, which was determined by UV-vis spectrophotometry. A typical calibration curve was plotted by linear fitting the absorbance values at wavelength length of 320 nm for various known concentration of 0.01, 0.02, 0.05, 0.1, 0.2, 0.3,

0.4, and 0.5 mmol L^{-1} of Ce^{4+} (Figure S22). The standard solution of Ce^{4+} with the concentration of 0.5 mmol L^{-1} was prepared by dissolving 16.65 mg of $Ce(SO_4)_2$ in 100 mL of 0.5 mol L^{-1} H_2SO_4. To quantify the produced H_2O_2, sample solution was mixed with 0.5 mmol L^{-1} Ce^{4+} solution by a volume ratio of 1:400 or 1:800. After standing for 2 hours, the mixture solution was then measured by UV-vis spectrophotometry. The yield of H_2O_2 was finally determined based on the reduced Ce^{4+} concentration. For the anode product, the concentration of the produced 2-furoic acid was determined by HPLC equipped with an UV-vis detector. A mixture of ammonium acetate (70%) and methanol (30%) was used as the mobile phase with a flow rate of 0.6 mL min^{-1}. The wavelength of the detector was set to 245 nm.

The faradaic efficiency (FE) for H_2O_2 generation in flow cell was calculated as follows:

$$FE(\%) = \frac{mole\ of\ generated\ H_2O_2 \times 2 \times 96,485}{total\ consumed\ charge\ (C)} \times 100\%$$

The FU conversion rate was calculated as follows:

$$Conversion\ rate_{FU}\ (\%) = \frac{mole\ of\ consumed\ FU}{mole\ of\ initial\ FU} \times 100\%$$

The FA yield rate were calculated as follows:

$$Yield\ rate_{FA} = \frac{C \times V}{A \times t}$$

where C is the concentration of the produced FA, V is the volume of the electrolyte in anode chamber, A is the area of the anode electrode, and t is the electrolysis duration.

Supporting Information

Supporting Information is available from the Wiley Online Library or from the author.

Acknowledgements

Conflict of Interest

The author declare no conflict of interest.

References

[1]   S. Siahrostami, A. Verdaguer-Casadevall, M. Karamad, D. Deiana, P. Malacrida, B. Wickman, M. Escudero-Escribano, E. A. Paoli, R. Frydendal, T. W. Hansen, I. Chorkendorff, I. E. L. Stephens, J. Rossmeisl, *Nat. Mater.* **2013**, *12*, 1137.

[2]   Z. W. Seh, J. Kibsgaard, C. F. Dickens, I. Chorkendorff, J. K. Norskov, T. F. Jaramillo, *Science* **2017**, *355*, eaad4998.

[3]   S. C. Perry, D. Pangotra, L. Vieira, L.-I. Csepei, V. Sieber, L. Wang, C. Ponce de León, F. C. Walsh, *Nat. Rev. Chem.* **2019**, *3*, 442.

[4]   J. M. Campos-Martin, G. Blanco-Brieva, J. L. G. Fierro, *Angew. Chem. Int. Ed.* **2006**, *45*, 6962.

[5]   S. Yang, A. Verdaguer-Casadevall, L. Arnarson, L. Silvioli, V. Čolić, R. Frydendal, J. Rossmeisl, I. Chorkendorff, I. E. L. Stephens, *ACS Catal.* **2018**, *8*, 4064.

[6]   S. Ranganathan, V. Sieber, *Catalysts* **2018**, *8*, 379.

[7]   A. Kulkarni, S. Siahrostami, A. Patel, J. K. Nørskov, *Chem. Rev.* **2018**, *118*, 2302.

[8]   M. Melchionna, P. Fornasiero, M. Prato, *Adv. Mater.* **2019**, *31*, 1802920.

[9]   Y. Jiang, P. Ni, C. Chen, Y. Lu, P. Yang, B. Kong, A. Fisher, X. Wang, *Adv. Energy Mater.* **2018**, *8*, 1801909.

[10]   C. Xia, Y. Xia, P. Zhu, L. Fan, H. Wang, *Science* **2019**, *366*, 226.

[11]   Z. Chen, S. Chen, S. Siahrostami, P. Chakthranont, C. Hahn, D. Nordlund, S. Dimosthenis, J. K. Nørskov, Z. Bao, T. F. Jaramillo, *React. Chem. Eng.* **2017**, *2*, 239.

[12]   C. H. Choi, M. Kim, H. C. Kwon, S. J. Cho, S. Yun, H.-T. Kim, K. J. J. Mayrhofer, H. Kim, M. Choi, *Nat. Commun.* **2016**, *7*, 10922.

[13]   D. Kim, H. Nam, Y.-H. Cho, B. C. Yeo, S.-H. Cho, J.-P. Ahn, K.-Y. Lee, S. Y. Lee, S. S. Han, *ACS Catal.* **2019**, *9*, 8702.

[14]   Y. L. Wang, S. Gurses, N. Felvey, A. Boubnov, S. S. Mao, C. X. Kronawitter, *ACS Catal.* **2019**, *9*, 8453.

[15]   A. Verdaguer-Casadevall, D. Deiana, M. Karamad, S. Siahrostami, P. Malacrida, T. W. Hansen, J. Rossmeisl, I. Chorkendorff, I. E. L. Stephens, *Nano Lett.* **2014**, *14*, 1603.

[16]   J. S. Jirkovský, I. Panas, E. Ahlberg, M. Halasa, S. Romani, D. J. Schiffrin, *J. Am. Chem. Soc.* **2011**, *133*, 19432.

[17]   Y. J. Sa, J. H. Kim, S. H. Joo, *Angew. Chem. Int. Ed.* **2019**, *58*, 1100.

[18]   Y. Liu, X. Quan, X. Fan, H. Wang, S. Chen, *Angew. Chem. Int. Ed.* **2015**, *127*, 6941.

[19]   S. Chen, Z. Chen, S. Siahrostami, T. R. Kim, D. Nordlund, D. Sokaras, S. Nowak, J. W. F. To, D. Higgins, R. Sinclair, J. K. Nørskov, T. F. Jaramillo, Z. Bao, *ACS Sustainable Chem. Eng.* **2018**, *6*, 311.

[20]   D. Iglesias, A. Giuliani, M. Melchionna, S. Marchesan, A. Criado, L. Nasi, M. Bevilacqua, C. Tavagnacco, F. Vizza, M. Prato, P. Fornasiero, *Chem* **2018**, *4*, 106.

[21]   T.-P. Fellinger, F. Hasché, P. Strasser, M. Antonietti, *J. Am. Chem. Soc.* **2012**, *134*, 4072.

[22]   L. Dai, Y. Xue, L. Qu, H.-J. Choi, J.-B. Baek, *Chem. Rev.* **2015**, *115*, 4823.

[23]   Y. Zheng, Y. Jiao, L. Ge, M. Jaroniec, S. Z. Qiao, *Angew. Chem. Int. Ed.* **2013**, *52*, 3110.

[24]   H. A. Hansen, V. Viswanathan, J. K. Nørskov, *J. Phys. Chem. C* **2014**, *118*, 6706.

[25]   Y. Jiao, Y. Zheng, M. Jaroniec, S. Z. Qiao, *Chem. Soc. Rev.* **2015**, *44*, 2060.

[26]   L. Li, H. Yang, J. Miao, L. Zhang, H.-Y. Wang, Z. Zeng, W. Huang, X. Dong, B. Liu, *ACS Energy Lett.* **2017**, *2*, 294.

[27]   Y. Jiao, Y. Zheng, M. Jaroniec, S. Z. Qiao, *J. Am. Chem. Soc.* **2014**, *136*, 4394.

[28]   G.-L. Chai, Z. Hou, T. Ikeda, K. Terakura, *J. Phys. Chem. C* **2017**, *121*, 14524.

[29]   S. Siahrostami, A. Verdaguer-Casdevall, M. Karamad, I. Chorkendorff, I. Stephens, J. Rossmeisl, *ECS trans.* **2013**, *58*, 53.

[30]   E. Wirnhier, M. B. Mesch, J. Senker, W. Schnick, *Chem. Eur. J.* **2013**, *19*, 2041.

[31]   P.-C. Hsu, H.-T. Chang, *Chem. Commun.* **2012**, *48*, 3984.

[32]   P. L. de Andres, R. Ramírez, J. A. Vergés, *Phys. Rev. B* **2008**, *77*, 045403.

[33]   J. Liu, Y. Zhang, L. Zhang, F. Xie, A. Vasileff, S.-Z. Qiao, *Adv. Mater.* **2019**, *31*, 1901261.

[34]   W. Ding, Z. Wei, S. Chen, X. Qi, T. Yang, J. Hu, D. Wang, L.-J. Wan, S. F. Alvi, L. Li, *Angew. Chem. Int. Ed.* **2013**, *52*, 11755.

[35]   Y. Okamoto, *Appl. Surf. Sci.* **2009**, *256*, 335.

[36]   T. Xing, Y. Zheng, L. H. Li, B. C. C. Cowie, D. Gunzelmann, S. Z. Qiao, S. Huang, Y. Chen, *ACS Nano* **2014**, *8*, 6856.

[37]   C. Tang, H.-F. Wang, X. Chen, B.-Q. Li, T.-Z. Hou, B. Zhang, Q. Zhang, M.-M. Titirici, F. Wei, *Adv. Mater.* **2016**, *28*, 6845.

[38]   W. Zhang, S. Y. Bu, Q. H. Yuan, Q. Xu, M. Hu, *J. Mater. Chem. A* **2019**, *7*, 647.

[39]   R. Zhou, Y. Zheng, M. Jaroniec, S.-Z. Qiao, *ACS Catal.* **2016**, *6*, 4720.

[40]   H. W. Kim, M. B. Ross, N. Kornienko, L. Zhang, J. Guo, P. Yang, B. D. McCloskey, *Nat. Catal.* **2018**, *1*, 282.

[41]   Z. Lu, G. Chen, S. Siahrostami, Z. Chen, K. Liu, J. Xie, L. Liao, T. Wu, D. Lin, Y. Liu, T. F. Jaramillo, J. K. Nørskov, Y. Cui, *Nat. Catal.* **2018**, *1*, 156.

[42]   Y. Sun, I. Sinev, W. Ju, A. Bergmann, S. Dresp, S. Kühl, C. Spöri, H. Schmies, H. Wang, D. Bernsmeier, B. Paul, R. Schmack, R. Kraehnert, B. Roldan Cuenya, P. Strasser, *ACS Catal.* **2018**, *8*, 2844.

[43]   Y. Sun, S. Li, Z. P. Jovanov, D. Bernsmeier, H. Wang, B. Paul, X. Wang, S. Kühl, P. Strasser, *ChemSusChem* **2018**, *11*, 3388.

[44]   H. K. Jeong, H. J. Noh, J. Y. Kim, M. H. Jin, C. Y. Park, Y. H. Lee, *EPL* **2008**, *82*, 67004.

[45]   H. B. Yang, J. W. Miao, S. F. Hung, J. Z. Chen, H. B. Tao, X. Z. Wang, L. P. Zhang, R. Chen, J. J. Gao, H. M. Chen, L. M. Dai, B. Liu, *Sci. Adv.* **2016**, *2*, e1501122.

[46]   Y. Ye, A. Kawase, M.-K. Song, B. Feng, Y.-S. Liu, M. A. Marcus, J. Feng, E. J. Cairns, J. Guo, J. Zhu, *Nanomaterials* **2016**, *6*, 14.

[47]   Y. Jiao, Y. Zheng, K. Davey, S.-Z. Qiao, *Nat. Energy* **2016**, *1*, 16130.

[48]   D. Pacilé, J. C. Meyer, A. Fraile Rodríguez, M. Papagno, C. Gómez-Navarro, R. S. Sundaram, M. Burghard, K. Kern, C. Carbone, U. Kaiser, *Carbon* **2011**, *49*, 966.

[49]   S. K. Singh, K. Takeyasu, J. Nakamura, *Adv. Mater.* **2019**, *31*, 1804297.

[50]   C. V. Rao, C. R. Cabrera, Y. Ishikawa, *J. Phys. Chem. Lett.* **2010**, *1*, 2622.

[51]   D. Guo, R. Shibuya, C. Akiba, S. Saji, T. Kondo, J. Nakamura, *Science* **2016**, *351*, 361.

[52]   T. Kondo, S. Casolo, T. Suzuki, T. Shikano, M. Sakurai, Y. Harada, M. Saito, M. Oshima, M. I. Trioni, G. F. Tantardini, J. Nakamura, *Phys. Rev. B* **2012**, *86*, 035436.

[53]   A. M. Román, J. C. Hasse, J. W. Medlin, A. Holewinski, *ACS Catal.* **2019**, *9*, 10305.

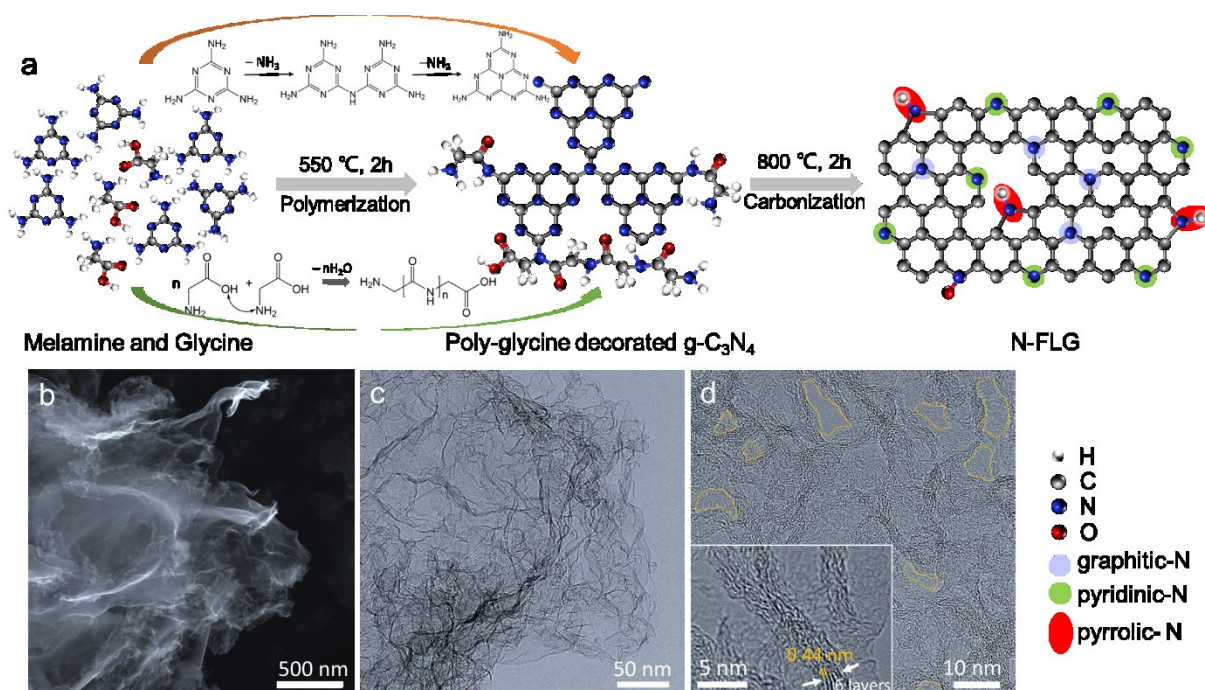[54]   X. Zhang, M. Han, G. Liu, G. Wang, Y. Zhang, H. Zhang, H. Zhao, *Appl. Catal. B* **2019**, *244*, 899.

Figure 1. Synthesis of N-FLG and structure characterization. a) Schematic illustration of the synthesis of N-FLG. b) SEM image of N-FLG-8. c) Low-resolution and d) high-resolution bright-field TEM images of N-FLG-8.
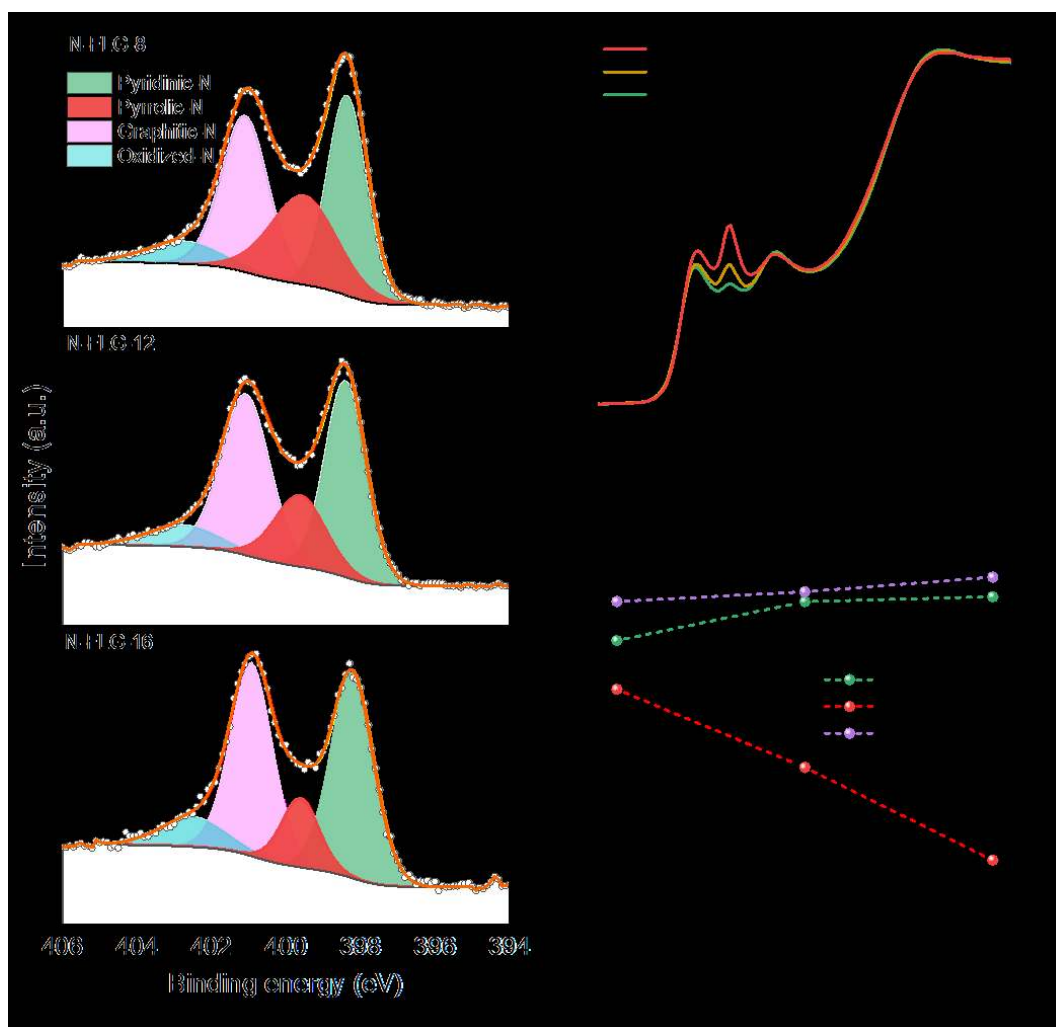
Figure 2. Composition investigation of N-FLG. a) High-resolution N 1s XPS spectra with peaks deconvoluted into pyridinic-N, pyrrolic-N, graphitic-N and oxidized-N species. b) XANES spectra of N-FLG-8, N-FLG-12 and N-FLG-16. c) The atomic contents of pyridinic-N, graphitic-N and pyrrolic-N for N-FLG-8, N-FLG-12 and N-FLG-16 derived from the XPS results.
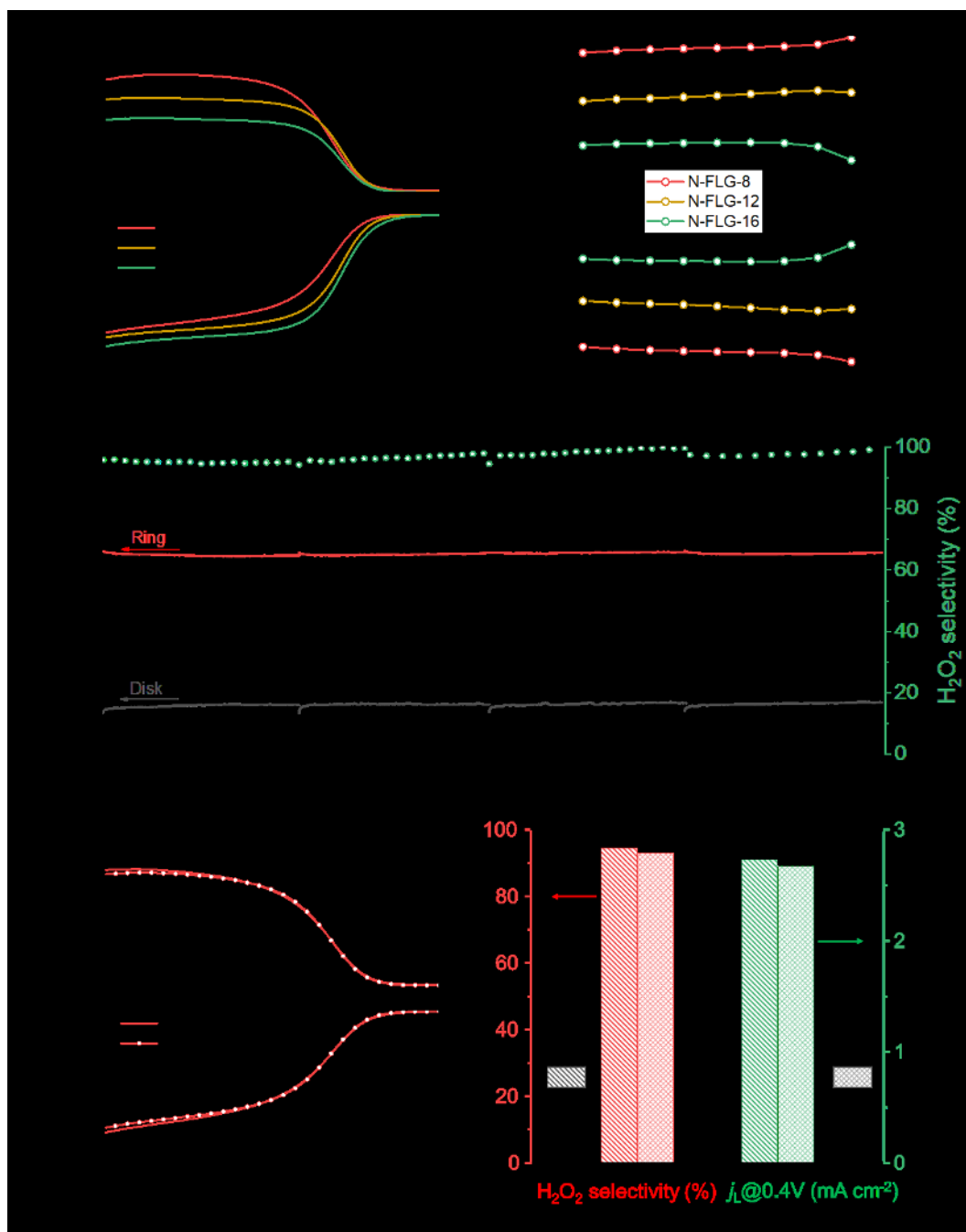
Figure 3. ORR performance of N-FLG in 0.10 M KOH. a) LSV curves of N-FLG-8, N-FLG-12 and N-FLG-16 recorded at 1600 rpm and at a rate of 5.0 mV s^{-1}, showing the ORR current density on the disk (j_{disk}) and the detected H_2O_2 currents on the ring electrode (I_{ring}). b) The calculated H_2O_2 selectivity and electron transfer number (n) during the potential sweep. c) Stability measurement of N-FLG-8 at a fixed disk potential of 0.40 V vs. RHE. The Pt ring was refreshed every 2 h by rapid scan at potential range from 0 to 0.8 V vs. RHE to remove the accumulated PtO$_x$, and the electrolyte was replaced to eliminate the influence of the accumulated H_2O_2 on the ring current during the continuous operation. d) LSV curves of N-FLG-8 and e) the H_2O_2 selectivity and diffusion-limiting disk current density (j_L) at 0.4 V vs. RHE before and after 8 h's stability test.
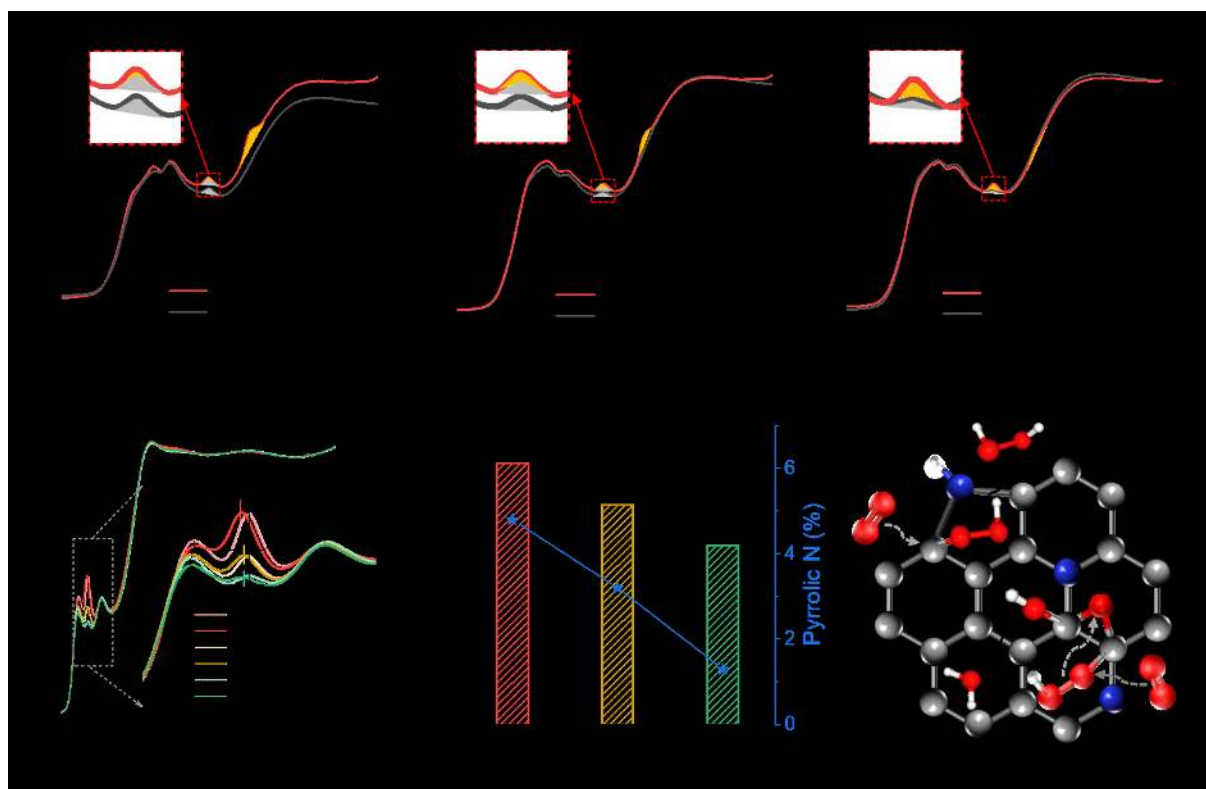
Figure 4. Elucidation of the activity origin for H_2O_2 generation. a-c) Carbon K edge and d) nitrogen K edge XANES spectra of N-FLG-8, N-FLG-12 and N-FLG-16 before and after ORR tests. In the insets of (a-c), the grey shadow presents the pristine peak before reaction and the orange shadow presents the peak increment after reaction. e) Relationship between H_2O_2 selectivity and atomic content of pyrrolic-N. f) Schematic diagram of two-electron and four-electron ORR pathways on N-FLG with different nitrogen configurations.
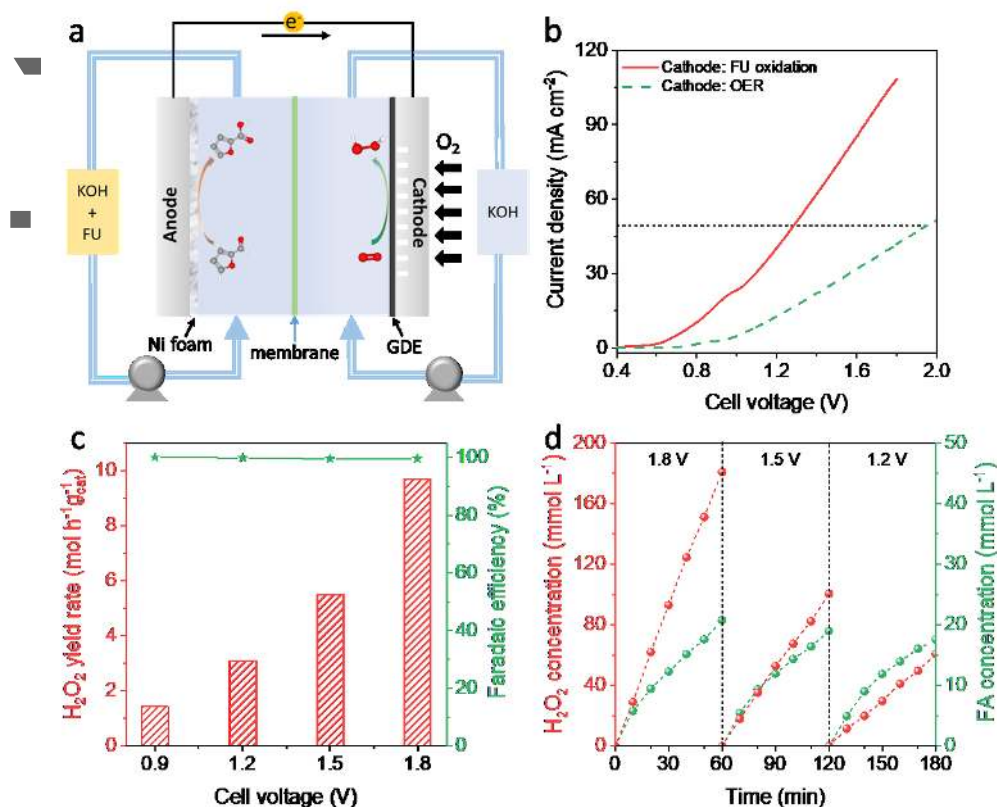
Figure 5. Application of N-FLG-8 in a practical flow cell device. a) Scheme of the flow cell coupling electrochemical furfural oxidation and H_2O_2 generation. b) LSV curves of the flow cell with or without furfural addition in the anode side. c) The H_2O_2 yield rates and faradaic efficiencies at different cell voltages. d) Stability test of the flow cell simultaneously generating 2-furoic acid and H_2O_2.